Numerical analysis on the influence of nozzles geometrical features on the combustion process of passive pre-chamber turbulent jet ignition engine

Original
Numerical analysis on the influence of nozzles geometrical features on the combustion process of passive pre-chamber turbulent jet ignition engine / Piano, Andrea; Scalambro, Andrea; Millo, Federico; Sementa, Paolo; Tornatore, Cinzia; Catapano, Francesco. - In: TRANSPORTATION ENGINEERING. - ISSN 2666-691X. - 19:(2025). [10.1016/j.treng.2025.100301]

Availability:
This version is available at: 11583/2996786 since: 2025-01-22T10:33:14Z

Publisher:
Elsevier Ltd

Published
DOI:10.1016/j.treng.2025.100301

Transportation Engineering 19 (2025) 100301

Contents lists available at ScienceDirect

Transportation Engineering

journal homepage: www.sciencedirect.com/journal/transportation-engineering

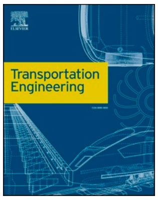

Full Length Article

Numerical analysis on the influence of nozzles geometrical features on the combustion process of passive pre-chamber turbulent jet ignition engine

Andrea Piano [a,*], Andrea Scalambro [a], Federico Millo [a], Paolo Sementa [b], Cinzia Tornatore [b], Francesco Catapano [b]

[a] Politecnico di Torino, corso Duca degli Abruzzi, 24, Torino, Italy
[b] Institute of Sciences and Technologies for Sustainable Energy and Mobility (STEMS), National Research Council, via Marconi, 4, Napoli, Italy

ARTICLE INFO

Keywords:
3D-CFD simulations
Pre-chamber
Turbulent jet ignition
Optimization

ABSTRACT

Engines equipped with pre-chamber technology offer a viable solution for extending the lean ignition limit, thanks to the high ignition energy delivered by the turbulent jets. Multidimensional numerical simulations are a valuable tool to speed up and support the development process of the system, by providing details that cannot be gathered solely from experimental tests. In this study, a 3D-CFD model was validated against experimental data under both stoichiometric and lean conditions in a gasoline engine equipped with a passive pre-chamber, featuring 4 nozzles, each with a 1.0 mm diameter. Afterward, three pre-chamber configurations with variable nozzle cross-sectional area and three geometries with constant nozzle area were analyzed. Among the nozzle configurations with variable cross-sectional area, the pre-chamber with an intermediate nozzle area (4 nozzles, 1.2 mm diameter) leads to the fastest combustion process, reducing combustion duration by 25% compared to the baseline pre-chamber. This is attributed to the improved pre-chamber scavenging, which increases the energy released in the pre-chamber by nearly 25%. This allows the generation of the most intense turbulence, hence increasing the charge entrained by the jets, and finally reducing combustion duration. Conversely, for excessively large total nozzle area (4 nozzles, 1.4 mm diameter), the enhanced scavenging effect is partially offset by the energy losses associated with the ejection of the cold jets, resulting in only a 10% increase in energy released in the pre-chamber compared to the baseline configuration. For the same total nozzle area, when a different number of pre-chamber nozzles is considered, the spatial distribution of the jets plays a crucial role in determining the combustion rate. Indeed, if the number of nozzles is excessively reduced (3 nozzles, 1.4 mm diameter), the consumption of the mixture located between two adjacent jets is delayed, increasing the combustion duration by almost 5% compared to the baseline and 40% compared to the optimal pre-chamber geometry (i.e., 4 nozzles, 1.2 mm).

1. Introduction

The 2023 Sixth Assessment Report (AR6) of the Intergovernmental Panel on Climate Change (IPCC) [1] states that greenhouse gas emissions related to human activity are the primary cause of global warming. With the long-term goal of becoming climate neutral by 2050 [2], the European Commission has set the target of reducing greenhouse gas emissions by 55% by 2030, compared to 1990 levels. At a global level, the transport sector accounts for a quarter of the total carbon dioxide emissions, 75% of which comes from road transportation [3]. Additionally, except for 2020 due to the pandemic, the overall amount of carbon dioxide emissions associated with the transport sector have been rising steadily [4] over the past few years. Therefore, because of the large impact of the transportation sector on greenhouse gas emissions, policymakers have set severe targets to be met over the next years. In particular, a reduction in carbon dioxide emissions of 15% by 2025 and 37.5% by 2030 is expected in the passenger cars sector. With this aim, the electrification of road vehicles seems to be one of the most promising pathways to achieve these objectives. Nonetheless, the time needed to massively electrify the fleet and some technical and economic barriers may hinder the rapid spread of this innovative solution [5]. Hence, internal combustion engine (ICE) powered vehicles are expected to play a predominant role until these barriers will be overcome [6]. In the last decade, several technical solutions such as turbocharging, direct

---

* Corresponding author.
E-mail address: andrea.piano@polito.it (A. Piano).

https://doi.org/10.1016/j.treng.2025.100301
Received 16 September 2024; Received in revised form 23 December 2024; Accepted 3 January 2025

injection, variable valve actuation, and downsizing, have been adopted for improving the efficiency of spark ignition (SI) engines. However, the strict targets that have to be achieved in the upcoming years require further efforts to improve brake thermal efficiency and reduce pollutant emissions. Lean combustion represents a valuable solution for filling this gap. Indeed, the reduction of the wall heat losses due to the decrease in the combustion temperature [7] and the increment of the specific heat ratios increase the thermodynamic efficiency. Moreover, the exploitation of lean mixtures allows the control of the load acting on the injected mass of fuel, reducing the negative pumping work [8], especially at part loads. Nevertheless, the increase in combustion duration and the unstable ignition process [9] of lean mixtures may reduce the potential benefits of such a solution to the point of seriously jeopardizing the correct operation of the engine.

Various high-energy ignition techniques (i.e., plasma ignition, laser-induced ignition, and pre-chamber ignition) have been proposed to mitigate the above-mentioned issues. Among them, pre-chamber ignition systems, enabling Turbulent Jet Ignition (TJI) operations have demonstrated excellent potential in increasing ignition energy, shortening the duration of combustion, and improving combustion stability [10,11]. This combustion system is made up of two separate chambers, named pre-chamber (PC) and main chamber (MC), connected through a series of nozzles. The spark plug ignites the pre-chamber mixture triggering combustion, thus increasing PC pressure. When the flame reaches the ducts that connect the two combustion chambers, hot turbulent jets develop in the main chamber acting as distributed ignition points. Pre-chamber ignition systems can be classified into two categories (active or passive) on the base of the approach exploited to form the PC mixture. In the passive pre-chamber concept, the entire mass of fuel involved in the combustion process (both combustion chambers) is injected either by a port fuel injection (PFI) or through a direct injection (DI) system in the MC. Therefore, the properties of the PC mixture are solely the result of the scavenging and filling processes that occur during the compression stroke. In contrast, an additional injector placed in the PC is used in the active pre-chamber to regulate the PC air-to-fuel ratio (AFR). This allows for decoupling the MC AFR from that of the PC, making possible the combustion of a stoichiometric mixture in the PC, which in turn was demonstrated to enhance the ignition performances and the MC combustion. Even though active pre-chamber system enables the extension of the lean limit to higher AFRs, passive systems are particularly suitable for automotive applications due to their smaller component count, easier installation, and lower cost [12].

Nevertheless, in passive pre-chamber systems, the lack of additional fuel injected into the pre-chamber makes the definition of its geometry fundamental for achieving high combustion stability and improving thermal efficiency. Indeed, the growth of the flame kernel and the flame propagation in the pre-chamber are heavily affected by the local conditions of the mixture, which in turn purely depend on the scavenging process. The majority of this process, governed by the pre-chamber geometrical characteristics, occurs during the compression stroke [12–14], reducing the time available for the fresh gases to reach the spark plug region. This adverse phenomenon is even magnified in low-load and high-speed conditions, as the scavenging process is slowed down [15–17], and for highly diluted mixtures because of the reduction of the total energy available in the pre-chamber [13]. Moreover, during the cold start phase, a larger amount of the pre-chamber energy is dissipated as heat through the cold surrounding walls, hindering flame propagation [18].

Pre-chamber design affects the combustion process in the main combustion chamber, too. Indeed, the ignition of the MC mixture is triggered by the jets that exit from the pre-chamber nozzles through chemical, thermal, and turbulent effects [19]. These jets convey hot and active species resulting from the combustion in the pre-chamber that act as multiple and distributed ignition points into the main chamber. Additionally, the highly turbulent nature of the jets favors their spread over a wide portion of the combustion chamber and increases the intensity of the turbulent flow field, enhancing the rate of combustion. Biswas et al. identified two ignition mechanisms namely jet ignition and flame ignition [20]. In the first mechanism, named jet ignition, the PC flame is quenched when passing through the nozzles, and the MC combustion is solely triggered by the chemical effects of the PC hot combustion products. As the orifice diameter increases, a jet of wrinkled turbulent flames containing incomplete combustion products can emerge in the MC (flame ignition), reducing the ignition delay. However, for too large orifice diameters, the reduction of the pressure difference between the pre- and main chamber decreases the jet velocity and the ejection process leads to a ‘mushroom clouds’ structure, in which the majority of the pre-chamber combustion products are delivered near the nozzle exit [21]. This leads to a lengthening of the combustion duration since the volume of the combustion chamber where the ignition takes place is quite small and located near the pre-chamber nozzles. On the contrary, smaller diameters generally lead to faster burn rates since higher jet velocity increases the turbulence level and distributes more uniformly to the ignition sites [21,22]. At the same time, for too small orifices, the negative effect due to nozzle flame stretch and heat losses, liner wall quenching, and the reduced jet dimension become predominant [23], increasing combustion duration. Besides the overall exchange area between PC and MC, also the number of nozzles has been shown to influence combustion duration [24]. Generally, a higher number of orifices leads to faster combustion processes since the combustion of premixed gases included between adjacent jets is promoted [25]. Therefore, the design of the ducts connecting the pre-chamber to the main combustion chamber is a multi-objective problem that requires keeping into account several heterogeneous phenomena. Recently, extensive research on pre-chamber ignition systems has been conducted with the aid of multi-dimensional numerical simulations, as they can provide detailed insights that cannot be obtained through experiments alone. These simulations, indeed, allow for a deeper understanding of combustion dynamics while reducing both costs and time, making them a valuable tool in optimizing pre-chamber designs and combustion processes. While a substantial body of literature exists on large-bore engines [26–30], there is relatively less research available on small engines used in automotive applications. In [31], the experimental data gathered from an active pre-chamber TJI system fuelled with methane were complemented with numerical simulations to gain a detailed view of both physical and chemical phenomena occurring in the pre-chamber and the main chamber. In [32], the development process of a scavenged pre-chamber for a similar application is reported, including both experiments and simulations. Nevertheless, the combustion process was modeled through a simplified approach which does not include detailed reaction kinetics. In [33], the same test case was exploited to assess the impact of different pre-chamber volumes on the combustion process, considering both stoichiometric and lean operating conditions. In [34], the gas-dynamic interactions between the two combustion chambers in an engine fuelled with gasoline were investigated through a three-dimensional numerical model relying on the Reynolds Averaged Navier-Stokes (RANS) equations. Additionally, two different nozzle diameters were numerically tested to assess the effect on pre-chamber scavenging, jet formation, and combustion. It was found that pre-chamber scavenging is improved with a larger nozzle area (A_{nozzle}), whereas smaller A_{nozzle} produces jets with higher velocity and longer penetration. Novella et al. [35], conducted a computational study to explore the limiting factors of the combustion process in a gasoline TJI engine. They found that pre-chamber scavenging is independent of the pre-chamber geometry as long as the ratio between A_{nozzle} and the pre-chamber nozzle remains within an acceptable range. Similarly, Liu et al. [36], examined the effects of pre-chamber design on the combustion process in a gasoline TJI engine, revealing that an optimized pre-chamber design enhances flame propagation while suppressing knock. However, few studies have systematically investigated the effects of varying nozzle configurations on the combustion characteristics in small engines for automotive applications, leaving the key design factors for system optimization still unclear. Therefore, in the present work, a three-dimensional computational fluid dynamics (3D-CFD) parametric study on the PC nozzle characteristics is performed to assess their effect on combustion performances and to define the key factors that have to be considered during the design definition of such combustion systems. The paper is organized as follows: first, the validation of the numerical model against experimental data is presented in two operating conditions (stoichiometric and lean). Then, starting from the nozzle configuration used in the experimental campaign, a sensitivity analysis of the total nozzle cross-sectional areas (sweep of nozzle diameter at constant nozzle number) and nozzle diameter (sweep of nozzle number at constant cross-sectional area) is performed. Specifically, the paper will initially focus on the analysis of pre-chamber combustion and then on the evolution of the combustion process in the main chamber, highlighting the effects that different nozzle structures have on the behavior of the turbulent jets, and therefore on the ignition process and burn rate of the main chamber mixture. The experimental activity was carried out at CNR STEMS laboratories in Naples, while numerical simulations were performed at the HPC@POLITO, the High-Performance Computing Center of the Politecnico di Torino.

2. Case study

2.1. Engine specifications

The experimental study was conducted on a single-cylinder naturally aspirated gasoline metal engine whose main geometrical parameters are reported in Table 1. The original conventional SI engine has a compression ratio of 11.5 and features a 4-valve pentroof combustion chamber with a central spark plug and a side housing for the injector, to enable direct injection operations.

The pre-chamber was properly designed to replace the central spark plug. It has a volume of 2.2 cm^3, which corresponds to 7.2% of the clearance volume (V_C). Therefore, the original compression ratio (CR) of 11.5 is lowered to 10.5 when the system is equipped with pre-chamber. The PC exploited for the experimental campaign has 4 nozzles with a diameter and a length of 1 mm, which target the jets in between the four valves. The total A_{nozzle} to pre-chamber volume ratio ($A_{nozzle}\ /V_{PC}$) is usually exploited to characterize PC geometry. In this case study, the noticeably large V_{PC} leads to a reduction of the A_{nozzle}/V_{PC} up to 0.017, a value well below what is commonly found in the literature [37].

As shown in Fig. 1, the PC is made up of an elongated cylindrical section (bottom), and a portion of a truncated cone (up). The cylindrical portion is characterized by a high length-to-diameter ($L\ /D$) ratio to avoid any interference of the pre-chamber with the intake ports and the engine cooling jacket. The upper section of the pre-chamber features a larger diameter to allow the installation of both the spark plug and an additional injector to operate the system in active mode too (not used in the present study). Due to these geometrical constraints, the spark is located in a region where the replacement of the residual gases by the fresh mixture is particularly challenging. This aspect is exacerbated by the low A_{nozzle}/V_{PC} ratio which further hinders the overall scavenging and filling of the PC. Therefore, all things considered, the geometry of the adopted PC results to be particularly appropriate for the optimization procedure covered in the present study. The geometrical characteristics of the pre-chamber are summarized in Table 2.

Table 1

Engine specifications.

Displacement	[cm^3]	250
Bore	[mm]	72
Stroke	[mm]	60
Compression Ratio	[-]	11.5 (SI) 10.5 (TJI)
Max Power	[kW]	16 @ 8000 rpm
Max Torque	[Nm]	20 @ 5500 rpm

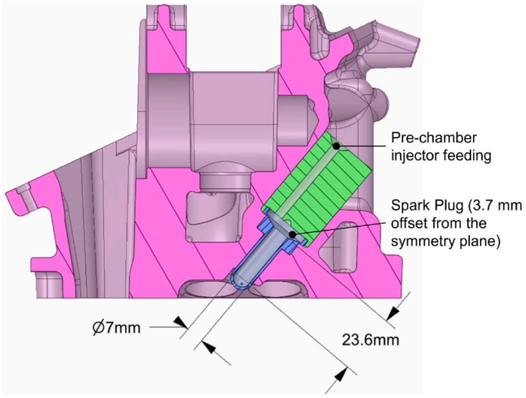

Fig. 1. Cross-sectional view of the main combustion chamber (hot pink), pre-chamber (grey), injector, and spark plug housing (green).

2.2. Working conditions

In this research activity, experimental and numerical investigations were carried out on two working points on the wide-open throttle (WOT) curve at medium-high engine speed. For each of the two operating conditions, 400 consecutive engine cycles were acquired to minimize the effects of cycle-to-cycle variations, a value consistent with those commonly reported in the literature [38–40]. In these operating conditions, the limited time available for the PC scavenging and filling could severely jeopardize combustion stability to the point of making the operation of a passive pre-chamber system [41] unfeasible. As shown in Table 3, when the engine is operated under stoichiometric conditions, an acceptable cycle-to-cycle variability is achieved, as highlighted by the IMEP coefficient of variation (COV_{IMEP}) which is lower than 1%. Nonetheless, as the AFR increases to 1.2, a considerably large spark advance (SA) is needed to guarantee a suitable phasing of MC combustion because of the lowering of the flame propagation speed. Therefore, combustion is triggered when a large amount of residual gases is still present inside the pre-chamber, thus hindering combustion stability, and resulting in higher COV_{IMEP} ($COV_{IMEP} > 2\%$). In this working point, higher AFRs were not investigated since vehicle driveability issues usually result when COV_{IMEP} exceeds about 2 to 5%, depending on engine operating conditions [42].

The instrumentation used in the experimental campaign is reported in Table 4, along with the accuracy and range of the instruments.

2.3. Test matrix

To study the impact of the geometrical features of the nozzles on the system behavior, a test matrix was defined (Table 5) as a function of the number and diameter of the nozzles. Starting from the base configuration of the pre-chamber with 4 circular nozzles with a diameter of 1.0 mm, two additional configurations with the same number of nozzles, but different diameters were tested (central column of Table 5). Specifically, the base diameter of 1.0 mm was increased by 20% and 40%. The choice of increasing the nozzle diameter was driven by the significantly low nozzle total cross-sectional area to pre-chamber volume ratio of the

Table 2

Pre-chamber geometrical specifications.

	[cm^3]	2.2
V_{PC}/V_C	[%]	7.2
Number of nozzles	[-]	4
Nozzle diameter	[mm]	1
A_{nozzle}/V_{PC}	[cm^{-1}]	0.017
L/D	[-]	3.4

Table 3
Operating conditions at 4000 rpm considered for the numerical analysis.

4000 rpm	IMEP [bar]	COV_{IMEP} %	Spark timing [CA aTDCf]
WP #1 Lambda 1.0	9.71	0.785	−25
WP #2 Lambda 1.2	8.73	2.32	−69

Table 4
Experimental instrumentation used in the study, with their respective range and accuracy specifications.

Parameter	Instrumentation	Range	Accuracy
Cylinder Pressure	Pressure transducer AVLGH1D	0 – 150 bar	–
Crank Angle	Angle Encoder AVL364	600 – 6000 rpm	± 0.02 deg
Air Mass Flow rate	Sensicon SensyFlow DN25	0 – 60 kg/h	± 0.4 kg/h
Fuel Consumption	Oval Gear flow meter VZS-005-VA	0.005 – 1.5 L/m	± 1.5 %
Lambda	Bosch LSU 4.9	0.8 – 1.7	± 0.05

Table 5
Total nozzle area to pre-chamber volume ratio ($\boldsymbol{A_{nozzle}/V_{PC}}$) for the tested geometrical configurations expressed in cm^{-1}.

		Number of nozzles		
		6	4	3
Diameter [mm]	1.0	0.0245	0.0170	
	1.2		0.0245	
	1.4		0.0334	0.0245

original configuration, compared with most of the values available in the literature [30,43–45]. In this way, the base A_{nozzle}/V_{PC} ratio was increased from 0.0170 cm^{-1} to 0.0245 cm^{-1} and 0.0334 cm^{-1} for the pre-chambers with a diameter equal to 1.2 mm and 1.4 mm, respectively. Then, two additional pre-chamber configurations with constant A_{nozzle} were tested. To do this, the number and the diameter of the nozzles were simultaneously varied. Overall, three pre-chambers with constant A_{nozzle} were designed. One of these, i.e. pre-chamber with 4 nozzles and a diameter of 1.2 mm, is in common with the previous set. The remaining two pre-chambers have 6 and 3 nozzles, with a diameter of 1.0 mm and 1.4 mm, respectively, and are displayed on the diagonal of Table 5. To simplify the reference to each pre-chamber geometry, the following naming convention will be employed: D ⟨Diameter of the single nozzle expressed in tens of mm⟩, N ⟨Number of nozzles⟩. For example, the base geometrical configuration with 4 nozzles, each of them with a diameter equal to 1.0 mm, will be referred to as D10N4.

Regarding the simulation methodology, a sweep of spark timing was performed to achieve the same combustion anchor angle (i.e. the MFB50) for all the tested configurations. The large range of $A_{nozzle}\ /V_{PC}$ in this study would have allowed the optimization of the spark timing (ST) to achieve higher loads and efficiencies. Nevertheless, it was preferred to neglect possible effects due to the calibration of combustion phasing to assess the impact of the geometrical features of the nozzles on combustion performance solely due to thermodynamic effects.

3. Simulations

3.1. Numerical setup

The commercial software CONVERGE CFD v3.0 was employed to perform the numerical simulations. As far as the discretization of the computational domain is concerned, its patented cut-cell technique was adopted. Therefore, the volume was discretized through an orthogonal mesh, with a base grid size set equal to 2 mm, determined through a grid sensitivity analysis and consistent with the approach used in the authors' previous works [46,47]. Local mesh refinements, allowing to reach a minimum grid size of 0.125 mm, were added in the connecting ducts and the spark plug region. Additionally, the Adaptive Mesh Refinement (AMR) algorithm was exploited to automatically refine the mesh where large velocity and temperature gradients (i.e. boundary of the turbulent jets and flame front) develop. This approach made it possible to keep the total cell number between 700.000 (end of the compression stroke) and 3 million (beginning of the exhaust stroke), thus decreasing the computational costs, without compromising the accuracy of the simulation. A first-order implicit Euler scheme was used for temporal discretization with a variable time step limited by the convection Courant-Friedrichs-Lewy (CFL) number (1), diffusion CFL (2), and Mach CFL (50). Conservation equations were solved through the Pressure Implicit with Splitting Operator (PISO) algorithm of Issa [48] coupled with the Rhie-Chow scheme. Boundary conditions, in terms of pressure, temperature, and species concentrations were gathered from a 1D GT-SUITE engine model. The PFI injection event was not modeled, but the fuel was considered perfectly vaporized and homogeneously distributed when entering the system boundary (intake port side), and therefore directly included among the inflow species. Indeed, for engines with small displacement volumes equipped with PFI systems, the level of mixture homogeneity achieved just before combustion is quite high, making it unnecessary to accurately model the injection process. Additionally, such a hypothesis has been considered valid in light of the results obtained (Section 3.2). To account for the pre-chamber residuals, which might significantly affect engine operations, the entire pre-chamber volume was initialized using only combustion products resulting from the complete combustion in the pre-chamber of the previous engine cycle. A RANS approach was used, coupled with the renormalization group (RNG) k-ε model [49]. Among the various combustion models available, the SAGE detailed chemical solver [50] was adopted in the present work for a few reasons. First, this model is capable of accounting for multiple and distributed ignition sources, as it usually occurs in TJI engines. Second, for highly turbulent flow fields and in lean conditions (typical conditions of TJI operation), the combustion process could shift into combustion regimes where the flamelet-based models (e.g. G-equation and Extended Coherent Flamelet Model) may no longer be suitable, at least from a formal perspective [51]. Finally, the choice of a combustion model entirely based on detailed chemistry, which does not require the calibration of any particular combustion parameters, intrinsically favors the predictivity of the model, providing further robustness to the work. The properties of the gasoline used for the experimental tests were reproduced employing a Toluene Reference Fuel (TRF) made up of 71,36% toluene (C7H8), 6, 60% isooctane (C8H18), 22,04% n-heptane (C7H16), as proposed in [52]. The combustion mechanism developed by Wu et al., including 165 species and 839 reactions [53] was adopted to describe the combustion process. Finally, ignition was modeled through a two-step energy profile, to mimic the breakdown and the arc and glow phases.

3.2. Model validation

The bar chart reported in Fig. 2 displays the comparison between the experimental data and the simulation outcomes in terms of Peak Firing Pressure (PFP) and its angular phasing (CA_{PFP}), 50% of mass fraction burned (MFB50), and combustion duration (MFB10–90) for the two operating engine conditions under investigation highlighted in Table 3. The height of each white column is representative of the experimental median cycle, obtained by sorting the 400 consecutive cycles in ascending order of PFP. For each of the mentioned indices, the error bar ($\pm\ 2\sigma$) is also reported to depict the statistical variability. As already mentioned in Table 3, as the mixture is enleaned, the reduced scavenging induced by the advance of the ST and the more unstable ignition and combustion processes considerably enlarge the variability range. Even though the simulated combustion duration is slightly

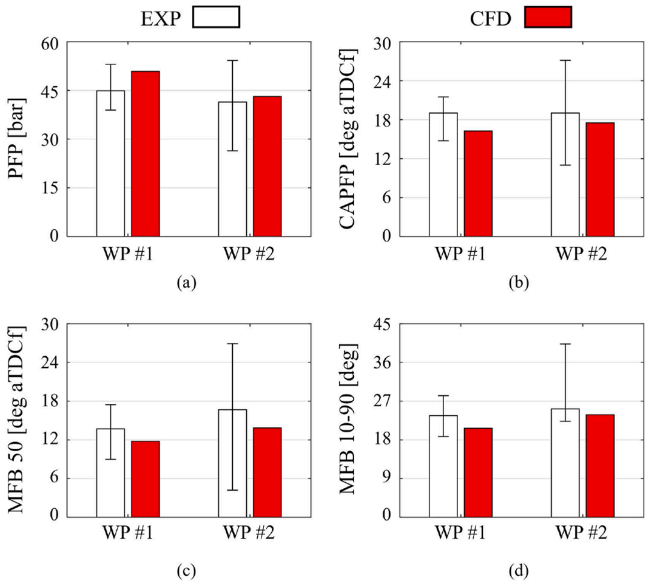

Fig. 2. Comparison between experimental median and numerical Peak Firing Pressure (a), Crank Angle of Peak Firing Pressure (b), Mass Fraction Burned 50 (c), Mass Fraction Burned 10–90 (d).

underpredicted in both operating conditions (Fig. 2d), numerical results fall within the experimental variability, indicating a general good agreement with the experiments. Moreover, the numerical model is capable of describing quite accurately the reduction of PFP, the increment of MFB50, and MFB10–90, and the delay of CA_{PFP} as the engine is operated with an excess of air. Therefore, the developed model is considered accurate enough to be exploited to perform a parametric study on the PC nozzles characteristics. Further details concerning model validation are reported in [54].

4. Results

Since the objective of the present work is not only to assess the impact of pre-chamber hole geometry but also to establish guidelines for the analysis of TJI combustion, only results corresponding to the stoichiometric working point are reported in this article. This choice is further supported by the fact that results obtained under both stoichiometric and lean conditions are nearly identical, exhibiting consistent trends, patterns, and responses to geometrical modifications.

4.1. Combustion analysis

Fig. 3 shows the evolution of PC and MC pressure and their difference along with the normalized Heat Release (HR) in MC and PC for the three geometrical configurations with variable A_{nozzle}. MC pressure is equal for the three tested configurations before the start of combustion (SoC), whereas PC pressure is lower than that of the MC and increases with the total A_{nozzle} thanks to the increased permeability of the pre-chamber. Therefore, a higher amount of fresh charge fills the PC, favoring a more efficient scavenging process which in turn should ensure a more stable combustion process. When combustion is triggered in the PC, the expansion of the hot burned gases causes pre-chamber pressure to rapidly increase, exceeding MC pressure. Initially, this leads to the ejection of cold jets (CJE) in the MC containing the mixture located in the lower portion of the PC. At a later time, as the flame reaches the connecting ducts, hot and chemically active jets develop in the MC, igniting the mixture, as confirmed by the rise of the HR curve. The pressure difference established between the two combustion chambers during PC combustion plays a fundamental role in determining the duration and intensity (speed) of the jets. A larger pressure difference is normally expected for smaller A_{nozzle} because of the lower PC permeability. In this specific case study, this trend is met for the pre-chambers D12N4 and D14N4, whereas a lower pressure difference is observed for the configuration D10N4. This can be ascribed to the advance of the phasing of the PC combustion which is needed to achieve the target MFB50. Indeed, the combination of the smaller total exchange area with the advance of the PC combustion, limits the scavenging, reducing the intensity of the combustion in PC. This causes a weaker build-up of PC pressure, which consequently reduces the intensity of the jets. Therefore, for pre-chamber D10N4 a substantial slowdown of MC combustion is noticed if compared to pre-chamber D12N4. Instead, pre-chamber D14N4 shows a similar combustion rate to that of D12N4 even though the lowest pressure difference is achieved. Indeed, the larger overall area of the connecting ducts is capable of outweighing the lower pressure difference, thus increasing the total mass flow rate of the jets which is delivered in the MC. To summarize, if the nozzles are excessively small, PC scavenging is reduced, which necessitates advancing the ST, ultimately resulting in slower burn rates.

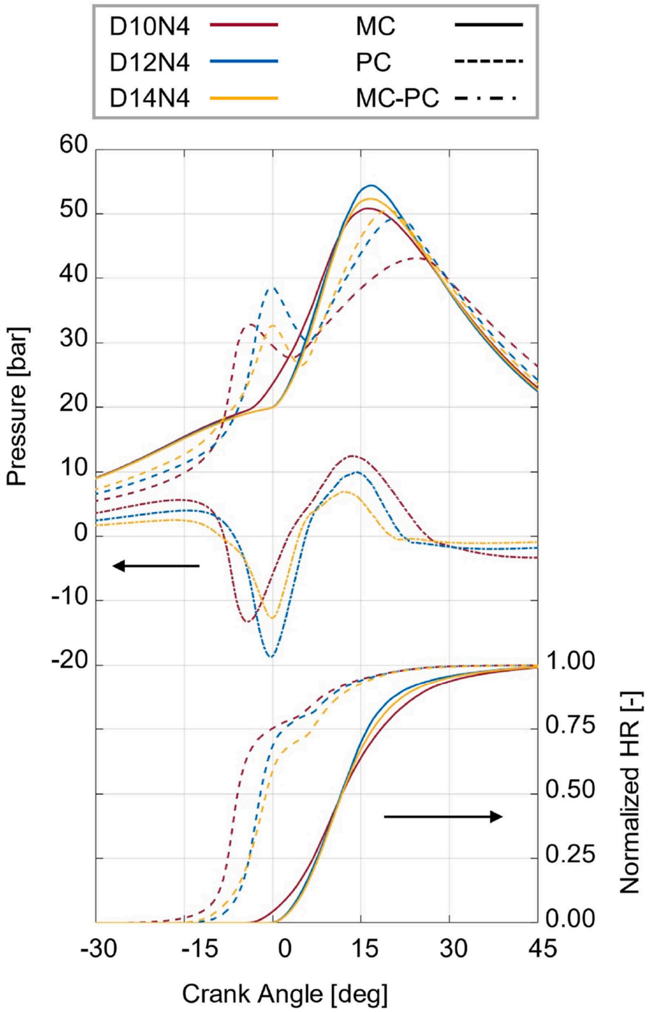

Fig. 3. Main chamber pressure, pre-chamber pressure, pressure relative difference (left axis), and normalized heat release (right axis) for the geometrical configurations with constant nozzle number and variable diameter (D10N4, D12N4, and D14N4).

When pre-chambers with constant A_{nozzle} are considered (Fig. 4), PC pressure is the same until the ST. Indeed, the equal exchange area between the two combustion chambers generates the same resistance to the passage of the mixture from the MC to the PC. Therefore, the same amount of fresh mixture is expected to fill the PC. Nonetheless, the different spatial interaction between the high-speed jets that enter the

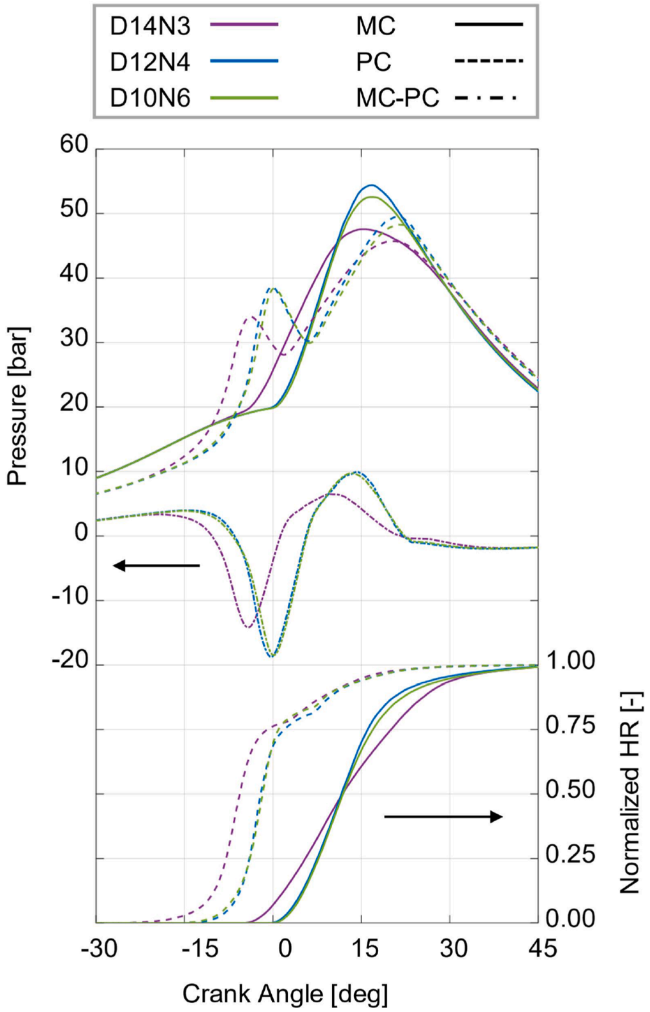

Fig. 4. Main chamber pressure, pre-chamber pressure, pressure relative difference (left axis), and normalized heat release (right axis) for the geometrical configurations with constant total nozzle area (D14N3, D12N4, and D10N6).

PC during the last phase of the compression stroke generates different turbulent flow fields, which in turn modify the local distribution of the residual gases. Pre-chamber D14N3 requires more advanced spark timing to achieve the target combustion anchor angle. Therefore, the scavenging process effectiveness is limited, thus lowering the amount of energy released in the PC and reducing the PC pressure rise. Accordingly, also the pressure difference between MC and PC is reduced, and hence MC combustion duration increases. On the other side, the similar evolution of PC combustion for pre-chambers D12N4 and D10N6 generates comparable PC pressure traces and MC combustion duration.

To enable a more quantitative assessment of the previously analyzed data, Fig. 5 presents the overall combustion durations (MFB0–90) for the five investigated configurations, systematically categorized into MFB0–10, MFB10–50, MFB50–75, and MFB75–90 phases. Among the pre-chambers with constant nozzle number (i.e., D10N4, D12N4, and D14N4), configurations D12N4 and D14N4 display a similar MFB0–90 (23.7 CAD, and 25.2 CAD for configurations D12N4, and D14N4, respectively), while for configuration D10N4 the MFB0–90 lasts 31.8 CAD. When considering pre-chambers with constant A_{nozzle} (i.e., D14N3, D12N4, and D10N6), pre-chamber D12N4 minimizes combustion duration (MFB0–90 = 23.7 CAD). Configuration D10N6 leads to a slightly slower combustion process (MFB0–90 = 25.2 CAD). The primary differences between these two configurations are concentrated in the last two combustion phases (i.e., MFB50–75 and MFB75–90), while the initial phases (i.e., MFB0–10 and MFB10–50) remain nearly constant. In contrast, configuration D14N3 significantly lengthens combustion (MFB0–90 = 32.9 CAD). Among all the configurations, D10N4 and D14N3 designs lead to significantly longer combustion processes, exhibiting increases of almost 35% and 40% compared to configuration D12N4, respectively. For these two configurations, the increment in combustion duration is distributed across all four combustion phases.

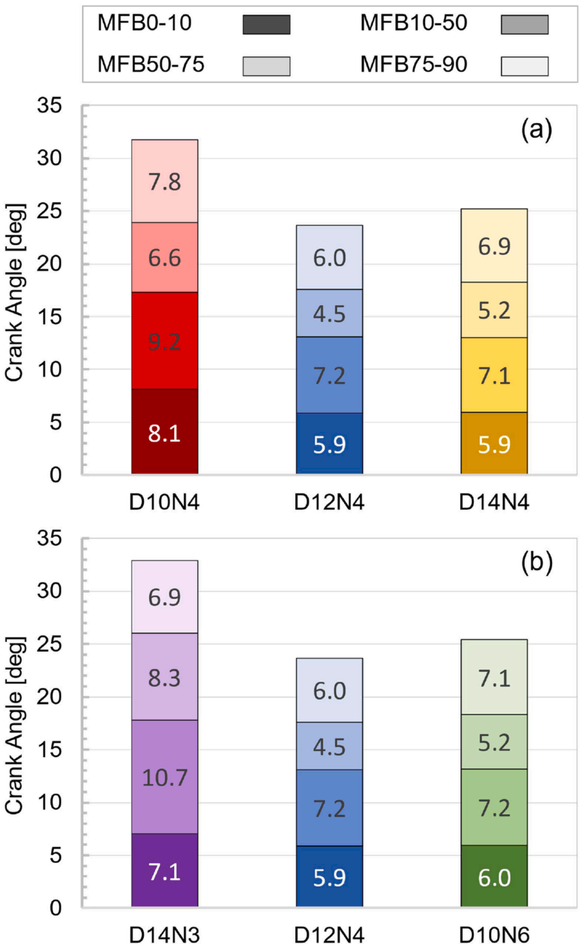

Fig. 5. Overall combustion duration (MFB0–90) split into MFB0–10, MFB10–50, MFB50–75, and MFB75–90 for constant pre-chamber nozzle number (a), and constant nozzle area (b).

In Sections 4.1 and 4.2, the combustion process occurring in the pre-chamber and main chamber is analyzed in detail, to provide a comprehensive explanation for the observed trends.

4.2. Pre-chamber combustion

A detailed analysis of PC combustion can be useful to explain the different evolutions of PC pressure shown in the previous section. Indeed, the pre-chamber is an open system that exchanges gases and energy with the MC before the SoC, during, and after the combustion in the PC has occurred. Hence, the evaluation of the total mass of fresh mixture that enters the PC before the SoC is not sufficient to characterize PC combustion, but a more accurate analysis is required. For this purpose, two different approaches were adopted in this study. The first method splits the PC energy into two contributions on a time basis, namely PC fuel power at ST (FP at ST) and PC fuel power before cold jet ejection (FP bCJE). Specifically, the PC energy at ST was computed as the mass of fuel in PC at ST multiplied by the fuel lower heating value (LHV). The same approach was exploited for evaluating the PC fuel power bCJE, although in that case, the start of cold jet ejection was used to identify the end of the measurement window. The term FP bCJE is representative of the PC combustion duration, while the sum with the term FP at ST provides a first estimation of the total amount of energy that enters the PC. Nonetheless, since not all the fuel that enters the PC is burned inside it, an additional analysis was performed. In particular, PC energy was divided into 5 contributions named:

- Heat Release before Hot Jet Ejection (HR bHJE) is computed as the cumulative energy released in PC before the appearance of the hot jets into the MC decreased by the pre-chamber wall heat transfer estimated within the same angular window
- Heat Release during Hot Jet Ejection (HR dHJE) is computed as the cumulative energy released in PC in the angular time frame that goes from the initial appearance of the hot jets into the MC until the End of the Ejection (EoE) process decreased by the pre-chamber wall heat transfer estimated within the same angular window
- Cold Jet Losses (CJL) is computed as the product between the fuel LHV and the mass of fuel that leaves the PC during the CJE phase
- Heat Losses (HL) are computed as the total heat transfer to the PC walls from the ST till the EoE
- Heat Release after HJE (HR aHJE) is representative of the energy released in the PC after the EoE, without considering the contributions due to the oxidation of partial combustion products that enter the PC after the EoE

Among the five mentioned terms, the first two are directly involved in increasing the energy of the jets that ignite the MC. The energy associated with the CJE does not help in triggering MC combustion but favors the early growth of MC turbulence. Instead, HL and HR aHJE do have not any beneficial effect on MC combustion and therefore have to be minimized.

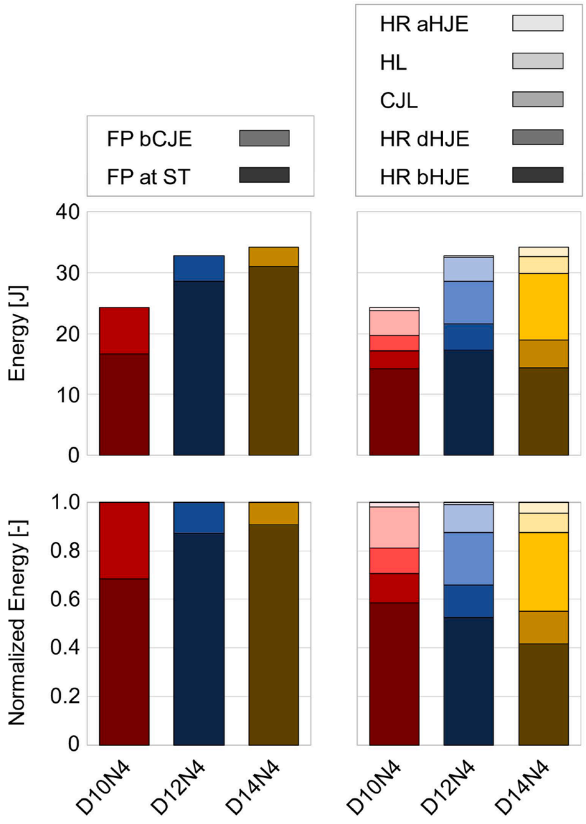

Fig. 6. Pre-chamber energy contributions (top) and normalized pre-chamber energy split (bottom) for the geometrical configurations with constant nozzle number and variable diameter (D10N4, D12N4, and D14N4).

Fig. 6 displays the pre-chamber energy split for pre-chambers with constant nozzle number and variable diameter following the above-mentioned definitions. In the left column PC energy is divided into PC energy at ST and PC energy bCJE, whereas in the right column in HR bHJE, HR dHJE, CJL, HL, and HR aHJE. Absolute values are reported in the top row and the normalized energy contributions are displayed in the bottom one. In accordance with the results shown in Fig. 3, the quantity of fresh mixture that fills the PC (i.e., PC at ST) rises with A_{nozzle} because the connecting ducts' resistance to the flow passage is reduced as the total A_{nozzle} grows. Indeed, for PC D10N4, the total amount of chemical energy which enters the pre-chamber during the scavenging and filling processes is equal to 24.3 J, while 32.8 J and 34.2 J for pre-chambers D12N4 and D14N4 respectively (i.e., +35% and +40% compared to the baseline PC). Additionally, the enhanced scavenging leads to a reduction in the duration of PC combustion. Hence, the total amount of chemical energy that enters the PC from ST until the start of the CJE reduces for a larger A_{nozzle} suggesting a faster PC pressure rise upon the ST. Moving to the analysis of PC combustion, it can be noticed that the highest overall ignition energy, given by the sum of the energy released before and during the ejection of the hot jets (HR bHJE and HR dHJE), is obtained for pre-chamber D12N4 and it corresponds to roughly 21 J, i.e. more than 2 orders of magnitude larger than the energy released by a conventional spark plug [55] (17.2 J and 18.9 J for PCs D10N4 and D14N4, respectively). For smaller A_{nozzle} (D10N4), the energy released in PC is limited by poor scavenging, while for a larger A_{nozzle} (D14N4) the higher permeability of the pre-chamber leads to an increase in the fuel that is pushed outside the PC within the cold jets, as shown by the CJL bar. As a matter of fact, while for PC D10N4, the energy lost due to the ejection of the cold jets corresponds to 10% of the total pre-chamber chemical energy, this term increases to 21% and 32% for PCs D12N4 and D14N4, respectively. Overall, only 70% of the pre-chamber fuel energy effectively contributes to the main chamber ignition for PC D10N4, 65% for PC D12N4, and 55% for PCD14N4, with the values obtained in the present study being well aligned with those reported in [35].

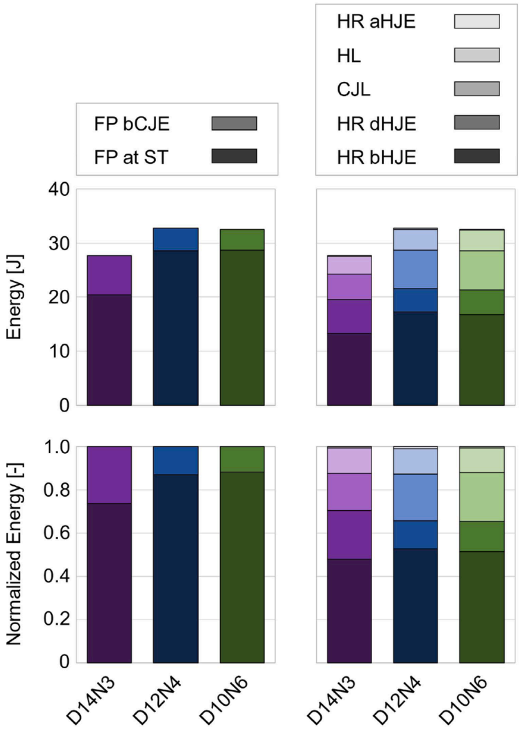

Fig. 7. Pre-chamber energy contributions (top) and normalized pre-chamber energy split (bottom) for the geometrical configurations with constant total nozzle area (D14N3, D12N4, and D10N6).

Fig. 7 shows the same PC energy breakdown described above but for the PC configurations with constant nozzle cross-sectional area. A sensible increase in the maximum PC chemical energy is observed for pre-chambers D12N4 and D10N6 compared to D14N3. This is due to the faster PC combustion that allows the delay of the ST, thus favoring the scavenging of the pre-chamber. Instead for the configuration D14N3, an advanced ST is required to keep fixed the combustion anchor angle as a result of the lowest combustion rate in MC, as reported in Fig. 4. Moreover, as highlighted by the FP bCJE term, pre-chamber D14N3 leads to the slowest PC combustion because of the worsening of the scavenging induced by the early ST. Differently from PC configurations with variable A_{nozzle}, here the losses of chemical energy conveyed by the cold jets are rather constant in relative terms, as expected (17%, 21%, and 22% of the total pre-chamber energy for PCs D14N3, D12N4, and D10N6, respectively). Finally, wall heat losses are similar both in absolute and relative terms for pre-chambers D12N4 and D10N6, while PC configuration D14N3 exchanges more heat with the surroundings because of the longer PC combustion duration. Therefore, taking everything into account and considering the highest ignition energy (sum of HR bHJE and HR dHJE), the D12N4 pre-chamber represents the optimal configuration among the tested geometries.

It is interesting to highlight how the different permeability of the pre-chambers influences the PC pressure evolution. Indeed, besides the pressure difference between the two combustion chambers, the number and the diameter of the PC nozzles impact the rate of pressure rise too. To quantitatively characterize this aspect, the derivative of the PC pressure was computed in the angular interval during which the turbulent jets develop and reported in Fig. 8. The pre-chamber with the smallest A_{nozzle} (i.e. D10N4) reaches the maximum value of the derivative of the PC pressure because of the lowest permeability that generates a strong resistance to the flow of the jets. At the same time, the geometry with the largest A_{nozzle} (i.e. D14N4) features a reduction in the peak value of the PC pressure derivative almost proportional to the increase in the A_{nozzle}. As reported in Fig. 6, these two geometries have comparable energy released in the PC. Therefore, the rate of pressure increase solely depends on the geometrical features of the connecting ducts. Additionally, the rate of pressure rise of pre-chamber D14N4 shows a two-step growth. First, it increases because of the rise of the pressure difference between the two combustion chambers. Then, when combustion is triggered in the PC, the expansion of the hot burned gases increases PC pressure, and the fast feeding of gases from the pre-chamber to the main chamber temporarily interrupts the rate of PC pressure rise. Finally, when the PC burning speed increases, pressure losses due to the ejection of the jets are more than outweighed by the pressure build-up generated by the expansion of the burned gases. Concerning the three pre-chambers with constant A_{nozzle}, the maximum value of the PC pressure derivative lies within a narrower band. Nonetheless, the fastest PC combustion in configuration D12N4 favors a faster PC pressure rise.

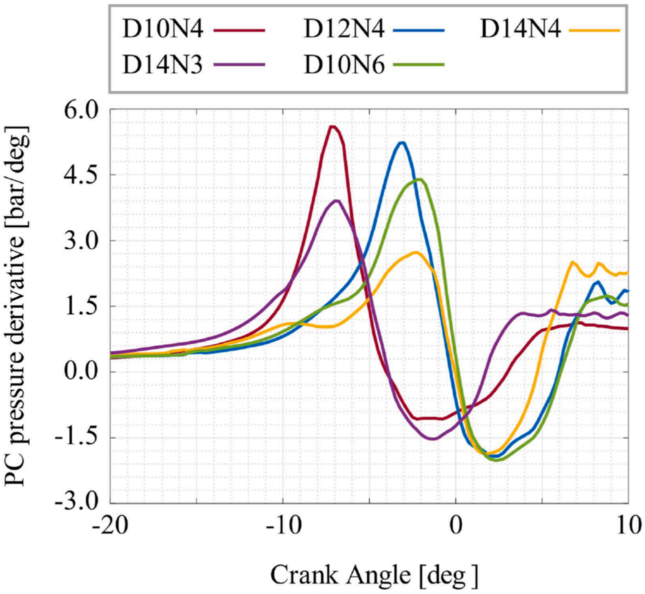

Fig. 8. Pre-chamber pressure derivative as a function of the crank angle for the 5 nozzle geometries.

4.3. Main chamber combustion

As previously stated, the ignition of the MC mixture is triggered by the hot turbulent jets that emerge from the pre-chamber nozzles. The turbulent jets contribute to the ignition of the MC charge through three mechanisms. Indeed, they continuously deliver in the MC high-temperature gases (thermal effect) containing reactive species (chemical effect), that result from the PC combustion and act as ignition sites. Additionally, they increase the turbulence intensity (turbulent effect) in the main combustion chamber, which helps in distributing the intermediate chemical species over a wider volume and speeding up the combustion process when the ejection process is over. A dedicated method was defined in [54] to quantify the impact of each contribution to the ignition and combustion of the MC. It consists of the split of the main chamber mass in 30 levels on the base of Turbulent Kinetic Energy (TKE), the temperature of the unburned gases, and the mass fraction of OH. In particular, the lower threshold of the turbulent intensity was defined to cut off any turbulent contribution generated by the intake process, whereas the upper bound was chosen to include the strongest turbulent fluctuation of the velocity field. From a thermal point of view, the analysis was focused only on the unburned gases. Therefore, the upper-temperature value was defined as equal to 950 K, and the mass of gases with a temperature higher than that was assigned to this level. Finally, the mass fraction of OH was exploited to determine the chemical contribution of the turbulent jets to the MC ignition and to assess combustion intensity. OH concentration was chosen for this purpose since it is not entirely consumed by the passage of the flame front, but it remains behind it until the oxidation reactions are completely over. Therefore, it is appropriate to indicate the mass of the MC mixture that is involved in the combustion process. For additional details concerning the interpretation of the plots below, please refer to [54].

Starting from pre-chamber D10N4 (Fig. 9(a)), three phases of the ignition process can be identified:

- Cold Jet Ejection (CJE) – The unburned gases that are located in the bottom section of the PC are pushed into the main combustion chamber by the expansion of the hot burned gases. The temperature of these jets is low and they do not contain either partial or complete products of combustion, as confirmed by the total lack of OH radicals (Fig. 8(a3)).
- Hot Jet Ejection (HJE) – The flame front in the PC has swept the entire PC volume and has reached the ducts that connect the two combustion chambers. The feeding of high-temperature gases increases MC temperature and effectively ignites the mixture. At this stage, two islands appear on the surface describing the evolution of the MC temperature (Fig. 9(a1)): the upper one identifies the portion of the MC gases that are directly entrained by the hot turbulent jets, thus immediately achieving a temperature higher than 950K. Instead, the diagonal trace is representative of the temperature of the gases that surround the jets and are heated through convection by them. Because of this, these gases do not quickly reach the highest temperature level, but the rate of temperature increase is determined by several parameters such as the temperature of the jets, their intensity, and spatial distribution. At the same time, the increase in the mass flow rate delivered from the PC into the MC favors the rapid growth of the turbulence intensity (Fig. 9(a2)) and the first appearance of OH radicals conveyed by the reactive jets is noticed (Fig. 9 (a3)).

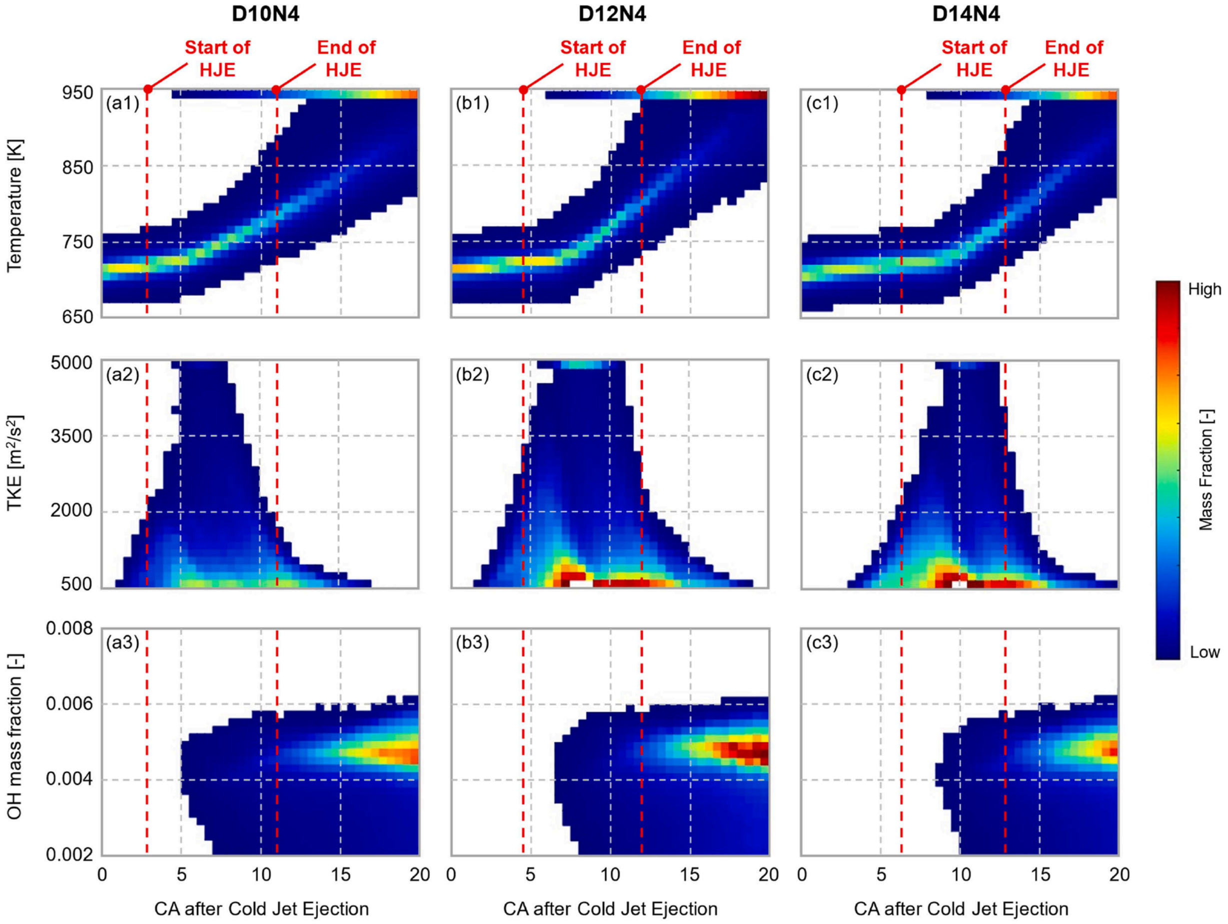

Fig. 9. Main chamber temperature (top), Turbulent Kinetic Energy (middle), and OH mass fraction (bottom) for the geometrical configurations with constant nozzle number (D10N4, D12N4, and D14N4).

- End of Hot Jet Ejection (EoHJE) – The ignition of the MC mixture by the HJE and the consequent progression of MC combustion increase MC pressure, putting an end to the HJE phase. Within this phase, MC unburned gases are consumed by the flame fronts which propagate from the boundary of the extinguished jets, achieving the highest temperature level (Fig. 9(a1)). This is confirmed by the trend of the OH mass fraction, which rapidly rises after the EoHJE (Fig. 9(a3)). Finally, the interruption of the mass delivered in the MC from the PC generates a reduction of the turbulent flow field intensity. Nonetheless, the decay of the most intense turbulence helps in sustaining turbulent motions to considerably high values long after the EoHJE, increasing combustion speed.

Fig. 9 displays the evolution of TKE, unburned gas temperature, and OH mass fraction for pre-chambers with variable A_{nozzle}, starting from the appearance of the cold jets. As the nozzle cross-sectional area (A_{nozzle}) increases, the duration of the CJE phases increases too, as highlighted by the delay of the temperature rise and OH mass fraction appearance. This is also confirmed by the MC temperature distribution shown in Fig. 10. Indeed, 5 crank angle degrees (CAD) after the start of the CJE phase (Fig. 10(a)), the hot jets are apparently visible only for pre-chamber D10N4. Instead, for pre-chambers D12N4 and D14N4, they are scarcely discernible and totally absent, respectively. However, the larger mass conveyed by the hot turbulent jets of pre-chamber D12N4 partially compensates for the delay induced by the lengthening of the CJE phase, as confirmed by the steeper temperature rise displayed in Fig. 9(b1). As a matter of fact, PC D12N4 displays the largest portion of MC volume entrained by the hot jets 10 CAD after CJE (aCJE) already (Fig. 10(b)). After the EoHJE (Fig. 10(c)-(d)), PC D12N4 shows a sensible faster growth of the flame front, compared to PC D10N4 and D14N4. This is probably due to the more intense turbulent flow field generated by this nozzle geometry (D12N4). As seen in the previous section, the geometrical configurations with a lower A_{nozzle} (D10N4) feature a faster development of the turbulent flow field, proportional to the PC rate of pressure rise, as highlighted by the larger TKE gradient (Fig. 9(b), left side of the figure). Nonetheless, the higher energy released in PC D12N4 favors the development of more intense jets, which in turn generate stronger turbulences. Fig. 11, showing MC TKE distribution, helps in understanding these two aspects also from a qualitative point of view. 5 CAD aCJE, the jets exiting from PCs D10N4 and D12N4 have a similar structure, made up of a highly turbulent core and a peripherical, less turbulent portion. In contrast, at the same time, the jets generated by geometry D14N4 are less developed, with a shorter penetration and an average lower turbulent intensity. Then, immediately before the EoHJE (10 CAD aCJE), the more intense combustion of PC D12N4 promotes the advancement of the turbulent jets far in the combustion chamber, closer to the cylinder liner. Finally, after the EoCJE (15 and 20 CAD aCJE), a single highly turbulent region, aligned with one of the four pre-chamber nozzles (top nozzle) is clearly visible for pre-chamber D10N4, while two (top and left nozzles) and three (top, left and bottom nozzles) of them are detectable respectively for configurations D14N4 and D12N4. Therefore, the more intense turbulent flow field noticed in PC D12N4 favors the reduction of the combustion duration by enhancing the speed of the turbulent flame propagation. This is indicated by the largest amount of OH mass fraction (Fig. 9(b3)) and also by the considerably highest mass of MC mixture with a temperature higher than 950 K (Fig. 9(b)) achieved for pre-chamber D12N4 (82%) 20 CAD aCJE, compared to D10N4 (65%) and D14N4 geometries

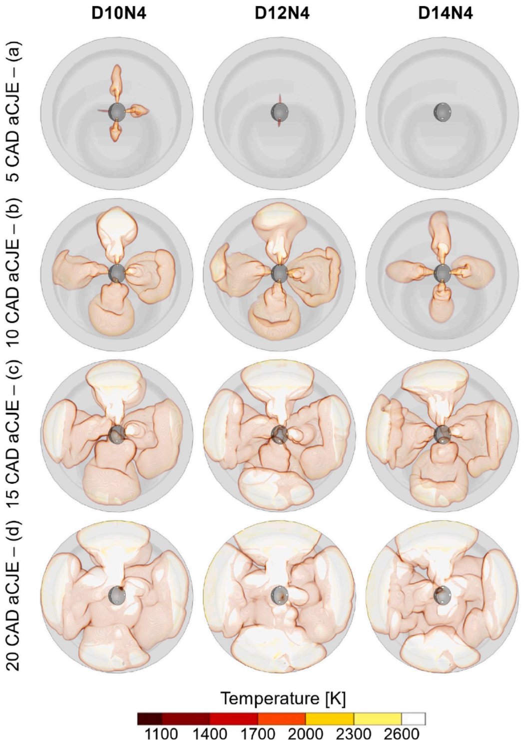

Fig. 10. Main chamber temperature distribution for the geometrical configurations with constant nozzle number (D10N4, D12N4, and D14N4).

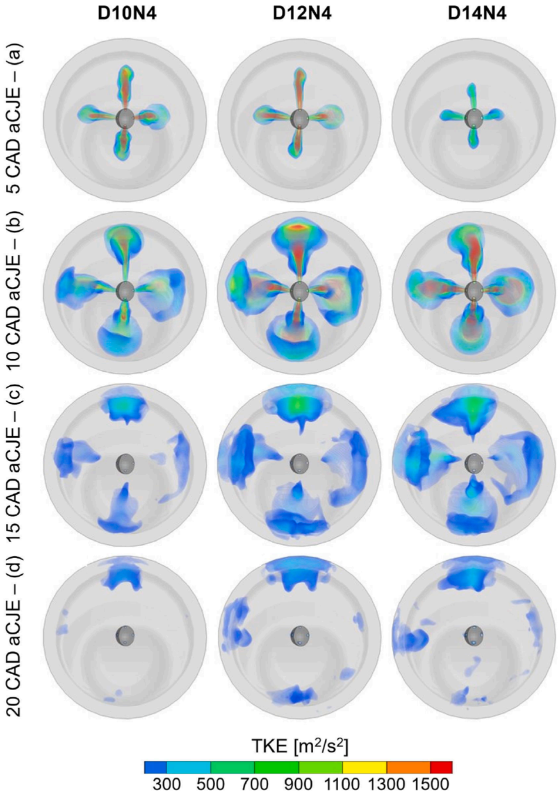

Fig. 11. Main chamber turbulent kinetic energy distribution for the geometrical configurations with constant nozzle number (D10N4, D12N4, and D14N4).

(67%).

Fig. 12 shows the evolution of TKE, unburned gases temperature, and OH mass fraction for pre-chambers with constant A_{nozzle}, starting from the appearance of the cold jets. Even though the permeability of these three geometries is constant, there are small differences in the duration of the CJE phase, as confirmed by the temperature distributions shown in Fig. 13(a). This is probably due to two concurrent effects. First, for pre-chamber D14N3 (shortest cold jet duration), the flame front could be located nearer to one of the PC nozzles when the CJE process begins, thus reducing the time needed by the flame to reach the MC. Second, a larger nozzle diameter induces a weak resistance to the passage of the flame through it, decreasing the probability of local flame quenching. During the HJE phase, the intensity of the turbulence generated by the jets exiting the PC is rather different among the tested pre-chambers. Because of the lower amount of fuel burned in pre-chamber D14N3, this geometry is not able to produce a turbulent flow field as intense as that generated by the other two configurations. Therefore, a reduced MC mass reaches the highest TKE levels. In contrast, pre-chambers D12N4 and D10N6 display a similar amount of energy released during PC combustion and thus a comparable overall TKE is obtained. Nonetheless, these two geometries show a different TKE allocation among the defined levels. In pre-chamber D12N4 the energy generated in the PC is distributed among four jets, while among six jets in PC D10N6. Therefore, a greater portion of the MC mass reaches the highest TKE level in the former, whereas in the latter a larger portion of the MC mixture is directly engulfed by the jets, thus favoring the development of a wider region with medium TKE intensity, but lowering the mass capable of reaching the highest turbulence level. Because of this effect, pre-chamber D10N6 is characterized by a faster decay of the turbulence intensity after the EoCJE, as also highlighted by the TKE distribution reported in Fig. 14(c)-(d). From a thermal perspective, besides the slightly different length of the CJE, the number of nozzles appears to affect the rate of temperature rise in the MC. For pre-chamber D14N3, MC temperature increases slower during the HJE phase, presumably because of the smaller energy released in PC. Then, after the EoHJE, the rate of temperature rise flattens out. This is due to the greater angular width between the PC nozzles which increases the time needed by the flame to consume the mixture located in between the nozzles. This is evidenced also in Fig. 13(c). Indeed, 15 CAD aCJE, the flame fronts resulting from the turbulent jets have already merged and are just about to join for pre-chamber D10N6 and D12N4 respectively, while are still rather distant for PC D14N3. Therefore 20 CAD aCJE, only 55% of the MC charge has reached a temperature higher than 950 K for PC D14N3, with a significant volume of the combustion chamber that has not yet been swept by the flame front (Fig. 13(d)). In contrast, the combustion progress is fairly similar for PCs D12N4 and D10N6, as suggested by the comparable temperature evolution (82% and 77% of the MC mass with a temperature higher than 950 K, respectively) and OH mass fraction.

In summary, the pre-chamber with the intermediate nozzle diameter (D12N4) leads to the fastest burn rate. This is well in agreement with what was reported in [56] in which pre-chambers characterized by different nozzle diameters were experimentally tested on the same engine fuelled with methane. Indeed, also in that study, it was found that an intermediate nozzle diameter, neither too big nor too small led to the shortest flame development angle.

5. Conclusions

A 3D-CFD numerical investigation was carried out to assess the impact of the geometrical features of pre-chamber nozzles on the combustion characteristics in a single-cylinder, naturally aspirated gasoline metal engine. By exploiting a 3D-CFD RANS model previously calibrated and validated against experimental data in two working conditions (stoichiometric and lean), a sensitivity analysis on the number and diameter of the pre-chamber nozzles was performed. Specifically, three geometrical configurations with variable nozzle cross-sectional area (fixed nozzle number and variable diameter) and three geometries with constant A_{nozzle} (variable nozzle number and diameter) were tested. The main findings can be summarized as follows:

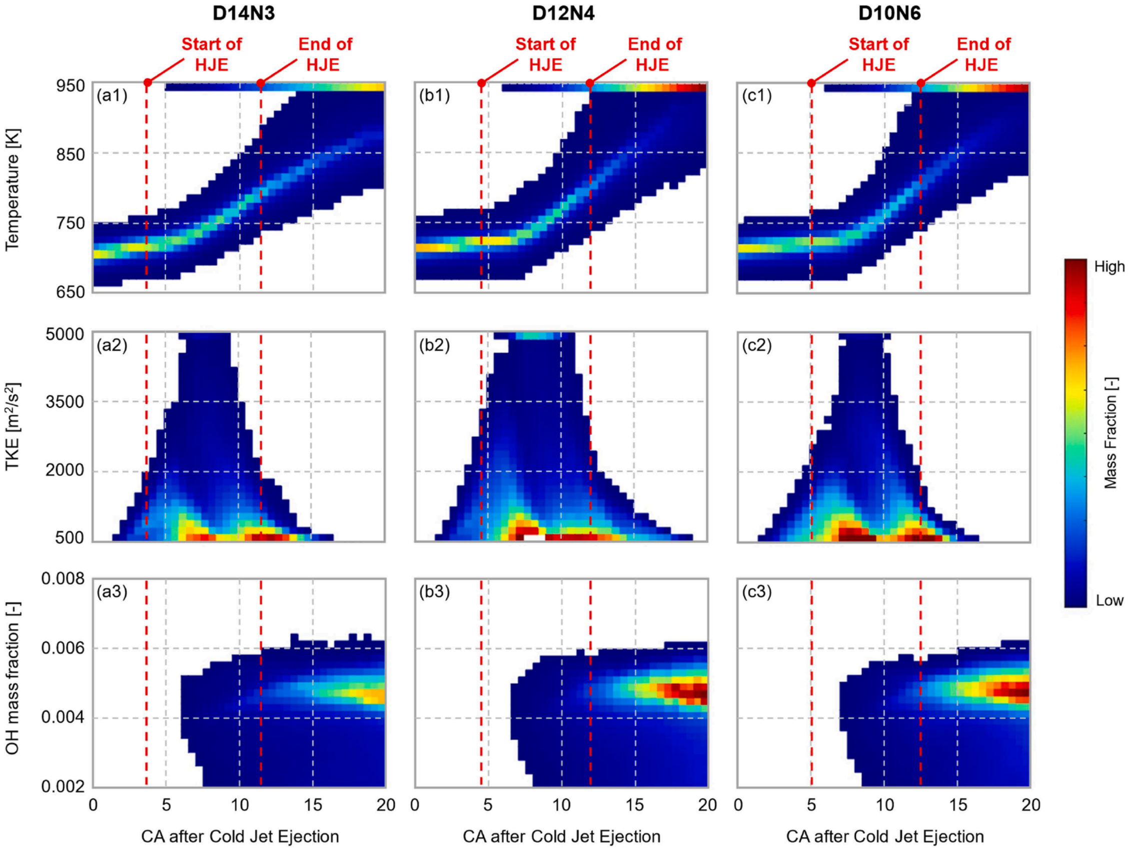

Fig. 12. Main chamber temperature (top), Turbulent Kinetic Energy (middle), and OH mass fraction (bottom) for the geometrical configurations with constant total nozzle area (D14N3, D12N4, and D10N6).

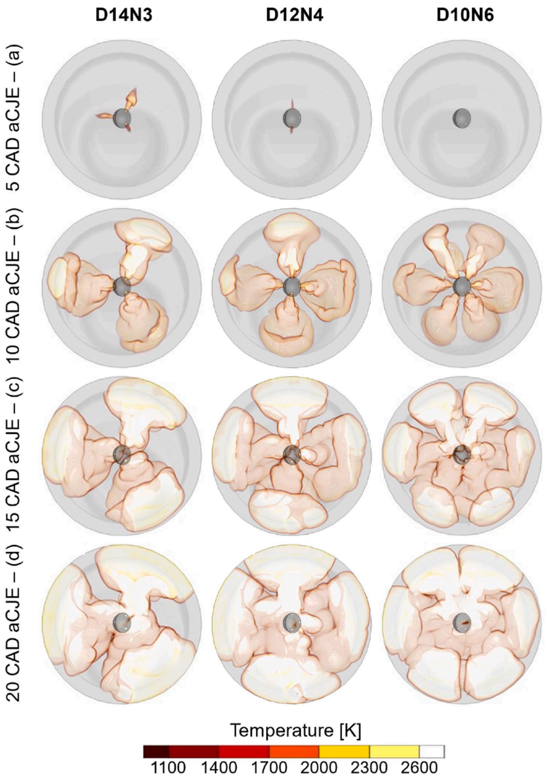

Fig. 13. Main chamber temperature distribution for the geometrical configurations with constant nozzle number and variable diameter (D10N4, D12N4, and D14N4).

- The design of the pre-chamber significantly affects combustion behavior. Among the 5 tested pre-chamber designs, prechamber D12N4 (4 nozzles, 1.2 mm) leads to a reduction of the combustion duration (MFB0–90) of 25% compared to the baseline pre-chamber D10N4 (4 nozzles, 1.0 mm) thanks to the increase of the energy released in the prechamber of nearly 25%, induced by the higher pre-chamber permeability.
- If the nozzle number is kept constant, further increasing the nozzle diameter to 1.4 mm (D14N4) results in only a marginal increase in the energy released in the pre-chamber (+10% compared to the baseline) mostly because of the air-fuel mixture that is pushed outside the pre-chamber when the pre-chamber pressure overcomes that of the main chamber, but the pre-chamber flame has not yet reached pre-chamber nozzles.
- If the total nozzle area is kept constant (i.e., D12N4, D10N6, D14N3) the energy released in the pre-chamber is almost constant, displaying a maximum deviation equal to 10%. This variation is primarily attributed to the different spark timings required to evenly phase the combustion process across the various pre-chamber designs. Indeed, as the spark timing is advanced, pre-chamber scavenging and filling processes are prematurely interrupted, thus reducing the mass of fresh mixture entering the pre-chamber.
- Although the energy released in the pre-chamber shows slight variations across different pre-chamber designs with a constant nozzle area (i.e., D12N4, D10N6, D14N3), significantly different combustion durations in the main chamber are observed. This is primarily due to the critical role that the spatial distribution of the jets plays in influencing the burning rate. The D14N3 pre-chamber design results in the longest combustion duration (MFB0–90 = 32.9 CAD), as the mixture directly entrained by the jets is reduced, and the consumption of the mixture located between adjacent jets is delayed.

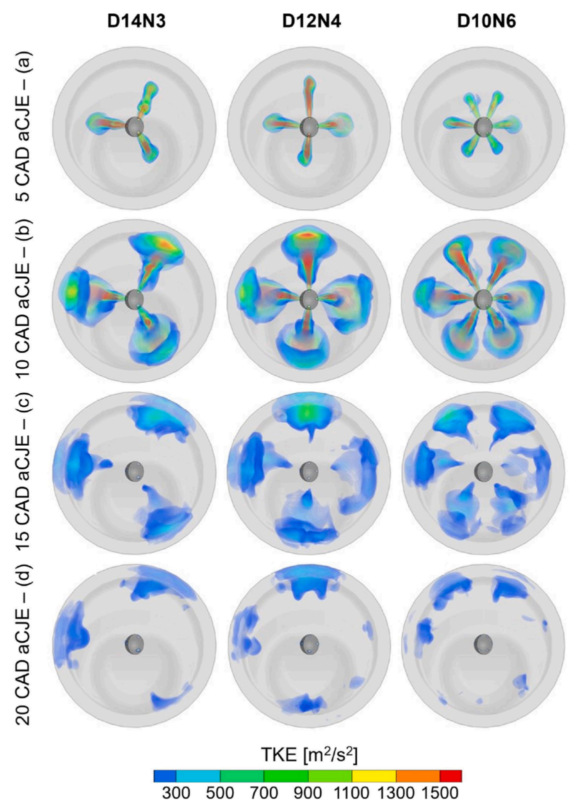

Fig. 14. Main chamber turbulent kinetic energy distribution for the geometrical configurations with constant nozzle number and variable diameter (D10N4, D12N4, and D14N4).

- Combustion durations for pre-chamber configurations D12N4 and D10N6, which have the same total nozzle area, are similar (MFB0–90 = 23.7 CAD for D12N4 and MFB0–90 = 25.4 CAD for D10N6). While no difference is observed in the MFB0–50 phase, the MFB50–90 phase is approximately 15% longer for the D10N6 pre-chamber. This is due to the more rapid decay of the turbulent flow field generated by the pre-chamber jets in the D10N6 configuration.

To complete the sensitivity analysis, a further study could assess the effect of pre-chamber volume on combustion performance. Additionally, combining the developed numerical model with data obtained from an optically accessible engine could provide further insights into the mechanisms governing main chamber ignition and the combustion process. This approach would allow for a more detailed examination of the interactions between the pre-chamber and the main combustion chamber, enabling a better understanding of the ignition dynamics. Furthermore, future research could extend this analysis to combustion systems that utilize carbon-neutral fuels. These fuels, including ammonia and synthetic fuels derived from renewable sources, could offer significant benefits in terms of reducing the carbon footprint of transportation systems. The application of the developed methodology to these alternative fuels would allow the optimization of the pre-chamber design pre-chamber for improving performance and efficiency while reducing pollutant emissions at the same time. This could provide valuable insights into enhancing the overall efficiency and reducing the environmental impact of the next generation of internal combustion engines, contributing to more sustainable transportation solutions.

Abbreviations/Acronyms

AMR	Adaptive Mesh Refinement
AFR	Air-to-fuel ratio
A_{nozzle}	Nozzle Area
CAD	Crank Angle Degrees
CFD	Computational Fluid Dynamics
CFL	Courant-Friedrichs-Lewy
CJE	Cold Jet Ejection
CJL	Cold Jet Losses
CR	Compression Ratio
DI	Direct Injection
EoE	End of the Ejection
EoHJE	End of Hot Jet Ejection
FP at ST	Fuel Power at ST
FP bCJE	Fuel Power before Cold Jet Ejection
HJE	Hot Jet Ejection
HL	Heat Losses
HR	Heat Release
HR aHJE	Heat Release after HJE
HR bHJE	Heat Release before Hot Jet Ejection
HR dHJE	Heat Release during Hot Jet Ejection
ICE	Internal Combustion Engine
LHV	Lower Heating Value
MC	Main Chamber
MFB10–90	Combustion Duration
MFB50	Combustion Anchor Angle
PC	Pre-chamber
PFI	Port Fuel Injection
PFP	Peak Firing Pressure
PISO	Pressure Implicit with Splitting Operator
RANS	Reynolds Averaged Navier-Stokes
RNG	Renormalization Group
SA	Spark Advance
SI	Spark Ignition
SoC	Start of Combustion
ST	Spark Timing
TJI	Turbulent Jet Ignition
TKE	Turbulent Kinetic Energy
TRF	Toluene Reference Fuel
V_c	Clearence Volume
V_{PC}	Pre-chamber Volume
WOT	Wide Open Throttle

(continued on next column)

(continued)

CRediT authorship contribution statement

Andrea Piano: Writing – review & editing, Supervision, Methodology, Conceptualization. **Andrea Scalambro:** Writing – original draft, Software, Methodology, Formal analysis. **Federico Millo:** Writing – review & editing, Supervision, Project administration. **Paolo Sementa:** Writing – review & editing, Resources, Investigation. **Cinzia Tornatore:** Writing – review & editing, Resources, Investigation. **Francesco Catapano:** Resources, Investigation.

Declaration of competing interest

The authors declare that they have no known competing financial interests or personal relationships that could have appeared to influence the work reported in this paper

Data availability

The data that has been used is confidential.

References

[1] P. Zhai. Sixth Assessment Report (AR6) of the Intergovernmental Panel on, Climate Change (IPCC), 2023.
[2] European Commission, “The European green deal”, Brussels, 2019.
[3] International Energy Agency, “Net zero by 2050 - a roadmap for the global energy sector,” 2021.
[4] IEA, Transport, IEA, Paris, 2022. https://www.iea.org/reports/transport. License: CC BY 4.0w w w.iea.org2022.

[5] G. Kalghatgi, Is it really the end of internal combustion engines and petroleum in transport? Appl. Energy 225 (2018) 965–974, https://doi.org/10.1016/j.apenergy.2018.05.076.

[6] World Energy Council., "Global transport scenarios 2050," ISBN 9780946121144, 2004.

[7] M. Aliramezani, I. Chitsaz, A.A. Mozafari, Thermodynamic modeling of partially stratified charge engine characteristics for hydrogen-methane blends at ultra-lean conditions, Int. J. Hydrog. Energy 38 (25) (2013) 10640–10647, https://doi.org/10.1016/j.ijhydene.2013.05.172.

[8] F. Ayala, M. Gerty, J. Heywood, Effects of Combustion Phasing, Relative Air-fuel Ratio, Compression Ratio, and Load on SI Engine Efficiency, SAE Technical Paper 2006-01-0229, 2006, https://doi.org/10.4271/2006-01-0229.

[9] Ayala, F. and Heywood, J., Lean SI Engines: The role of combustion variability in defining lean limits, SAE Technical Paper 2007-24-0030, 2007, https://doi.org/10.4271/2007-24-0030.

[10] P. Sementa, F. Catapano, S.Di Iorio, B.M. Vaglieco, Effects of prechamber on efficiency improvement and emissions reduction of a SI engine fuelled with gasoline, in: Proceedings of the *SAE Technical Papers*, SAE International, 2019, https://doi.org/10.4271/2019-24-0236.

[11] W.P. Attard, M. Bassett, P. Parsons, H. Blaxill, A new combustion system achieving high drive cycle fuel economy improvements in a modern vehicle powertrain, in: Proceedings of the *SAE World Congress and Exhibition*, 2011, https://doi.org/10.4271/2011-01-0664.

[12] R. Novella, J. Pastor, J. Gomez-Soriano, I. Barbery, C. Libert, F. Rampanarivo, C. Panagiotis, M. Dabiri, Experimental and numerical analysis of passive pre-chamber ignition with EGR and air dilution for future generation passenger car engines, in: Proceedings of the *SAE Technical Papers*, SAE International, 2020, https://doi.org/10.4271/2020-01-0238.

[13] J. Benajes, R. Novella, J. Gomez-Soriano, I. Barbery, C. Libert, F. Rampanarivo, M. Dabiri, Computational assessment towards understanding the energy conversion and combustion process of lean mixtures in passive pre-chamber ignited engines, Appl. Therm. Eng. 178 (2020), https://doi.org/10.1016/j.applthermaleng.2020.115501.

[14] G. Onofrio, P. Napolitano, P. Tunestål, C. Beatrice, Combustion sensitivity to the nozzle hole size in an active pre-chamber ultra-lean heavy-duty natural gas engine, Energy 235 (2021), https://doi.org/10.1016/j.energy.2021.121298.

[15] R. Novella, J. Gomez-Soriano, I. Barbery, C. Libert, Numerical analysis of the passive pre-chamber ignition concept for light duty applications, Appl. Therm. Eng. 213 (2022), https://doi.org/10.1016/j.applthermaleng.2022.118610.

[16] R. Novella, J. Gomez-Soriano, P.J. Martinez-Hernandiz, C. Libert, F. Rampanarivo, Improving the performance of the passive pre-chamber ignition concept for spark-ignition engines fueled with natural gas, Fuel 290 (2021), https://doi.org/10.1016/j.fuel.2020.119971.

[17] J.J. López, R. Novella, J. Gomez-Soriano, P.J. Martinez-Hernandiz, F. Rampanarivo, C. Libert, M. Dabiri, Advantages of the unscavenged pre-chamber ignition system in turbocharged natural gas engines for automotive applications, Energy 218 (2021), https://doi.org/10.1016/j.energy.2020.119466.

[18] M. Sens, E. Binder, Pre-chamber ignition as a key technology for future powertrain fleets, MTZ worldwide 80 (2) (2019) 44–51.

[19] M. Muller, C. Freeman, P. Zhao, H. Ge, Numerical simulation of ignition mechanism in the main chamber of a turbulent jet ignition system, in: Proceedings of the *Internal Combustion Engine Division Fall Technical Conference*, American Society of Mechanical Engineers, 2018.

[20] S. Biswas, S. Tanvir, H. Wang, L. Qiao, On ignition mechanisms of premixed CH4/air and H2/air using a hot turbulent jet generated by pre-chamber combustion, Appl. Therm. Eng. 106 (2016) 925–937, https://doi.org/10.1016/j.applthermaleng.2016.06.070.

[21] Shah, A. and Johansson, B., "CFD simulations of pre-hamber jets' mixing characteristics in a heavy duty natural gas engine," 2015.

[22] M. Bunce, H. Blaxill, W. Kulatilaka, N. Jiang, The effects of turbulent jet characteristics on engine performance using a pre-chamber combustor, in: Proceedings of the *SAE Technical Papers*, SAE International, 2014, https://doi.org/10.4271/2014-01-1195.

[23] B.C. Thelen, E. Toulson, A computational study on the effect of the orifice size on the performance of a turbulent jet ignition system, Proc. Inst. Mech. Eng. Part D J. Automob. Eng. 231 (4) (2017) 536–554, https://doi.org/10.1177/0954407016659199.

[24] L. Zhou, Y. Song, J. Hua, F. Liu, Z. Liu, H. Wei, Effects of different hole structures of pre-chamber with turbulent jet ignition on the flame propagation and lean combustion performance of a single-cylinder engine, Fuel 308 (2022), https://doi.org/10.1016/j.fuel.2021.121902.

[25] T. Wakasugi, D. Tsuru, H. Tashima, Influences of the pre-chamber orifices on the combustion behavior in a constant volume chamber simulating pre-chamber type medium-speed gas engines, Combust. Engines (2022), https://doi.org/10.19206/ce-148171.

[26] S. Eicheldinger, D.-I. Maximilian Prager, D.-I. Georg Wachtmeister, H. Dung Nguyen, D.-I. Sabine Dohrmann, K. Kuppa, F. Dinkelacker, BMEP >30 bar with gas engines, in: Proceedings of the *27th Aachen Colloquium Automobile and Engine Technology*, 2018.

[27] A. Shah, P. Tunestal, B. Johansson, Scalability aspects of pre-chamber ignition in heavy duty natural gas engines, in: Proceedings of the *SAE Technical Papers*, SAE International, 2016, https://doi.org/10.4271/2016-01-0796.

[28] A. Shah, B. Johansson, CFD simulations of pre-hamber jets' mixing characteristics in a heavy duty natural gas engine, in: Proceedings of the *SAE Technical Paper*, 2015.

[29] M. Wang, X. Leng, Z. He, S. Wei, L. Chen, Y. Jin, A numerical study on the effects of the orifice geometry between pre- and main chamber for a natural gas engine, in: Proceedings of the *SAE Technical Papers*, SAE International, 2017, https://doi.org/10.4271/2017-01-2195.

[30] A. Shah, P. Tunestal, B. Johansson, Effect of pre-chamber volume and nozzle diameter on pre-chamber ignition in heavy duty natural gas engines, in: Proceedings of the *SAE Technical Papers*, SAE International, 2015, https://doi.org/10.4271/2015-01-0867.

[31] E. Distaso, R. Amirante, E. Cassone, P.De Palma, P. Sementa, P. Tamburrano, B. M. Vaglieco, Analysis of the combustion process in a lean-burning turbulent jet ignition engine fueled with methane, Energy Convers. Manage 223 (2020), https://doi.org/10.1016/j.enconman.2020.113257.

[32] J. Vavra, Z. Syrovatka, O. Vitek, J. Macek, M. Takats, Development of a pre-chamber ignition system for light duty truck engine, in: Proceedings of the *SAE Technical Papers*, SAE International, 2018, https://doi.org/10.4271/2018-01-1147.

[33] Z. Syrovatka, O. Vitek, J. Vavra, M. Takats, Scavenged pre-chamber volume effect on gas engine performance and emissions, in: Proceedings of the *SAE Technical Papers*, SAE International, 2019, https://doi.org/10.4271/2019-01-0258.

[34] T. Yu, D.E. Lee, J.P. Gore, L. Qiao, Gas-dynamic interactions between pre-chamber and main chamber in passive pre-chamber ignition gasoline engines, SAe Int. J. Engines 17 (1) (2024) 135–149.

[35] J. Benajes, R. Novella, J. Gomez-Soriano, I. Barbery, C. Libert, F. Rampanarivo, M. Dabiri, Computational assessment towards understanding the energy conversion and combustion process of lean mixtures in passive pre-chamber ignited engines, Appl. Therm. Eng. 178 (2020), https://doi.org/10.1016/j.applthermaleng.2020.115501.

[36] S. Liu, Z. Lin, Y. Qi, G. Lu, B. Wang, Y. Liu, Z. Wang, Simulation investigation of Turbulent Jet Ignition (TJI) combustion in a dedicated hybrid engine under stoichiometric condition, in: Proceedings of the *SAE Technical Papers*, SAE International, 2024, https://doi.org/10.4271/2024-01-2111.

[37] P. Janas, N. Werner, Towards a thermally robust automotive pre-chamber spark plug for turbocharged direct injection gasoline engines, in: M. Günther (Ed.), Ignition Systems for Gasoline Engines: 4th International Conference, Berlin, Germany, 2018.

[38] H. Akçay, H. Gürbüz, Investigation of the effect of HHO-assisted flame-jet ignition on in-cylinder combustion, engine performance, and environmental indicators in a propane-fueled SI engine, Appl. Therm. Eng. 253 (2024), https://doi.org/10.1016/j.applthermaleng.2024.123730.

[39] X. Duan, B. Deng, Y. Liu, Y. Li, J. Liu, Experimental study the impacts of the key operating and design parameters on the cycle-to-cycle variations of the natural gas SI engine, Fuel 290 (2021), https://doi.org/10.1016/j.fuel.2020.119976.

[40] E. Zervas, Correlations between cycle-to-cycle variations and combustion parameters of a spark ignition engine, Appl. Therm. Eng. 24 (14–15) (2004) 2073–2081, https://doi.org/10.1016/j.applthermaleng.2004.02.008.

[41] J. Benajes, R. Novella, J. Gomez-Soriano, P.J. Martinez-Hernandiz, C. Libert, M. Dabiri, Evaluation of the passive pre-chamber ignition concept for future high compression ratio turbocharged spark-ignition engines, Appl. Energy 248 (2019) 576–588, https://doi.org/10.1016/j.apenergy.2019.04.131.

[42] J. Heywood, Internal Combustion Engine Fundamentals 2E, 2nd edition, McGraw-Hill Education, New York, 2019.

[43] F.Di Sabatino, P.J. Martinez-Hernandiz, R. Novella Rosa, I. Ekoto, Investigation of the effects of passive pre-chamber nozzle pattern and ignition system on engine performance and emissions, Int. J. Engine Res. 24 (6) (2023) 2592–2613.

[44] J. Krajnović, M. Sjerić, R. Tomić, D. Kozarac, A novel concept of active pre-chamber engine with a single injector – the passive main chamber approach, Appl. Therm. Eng. 250 (2024), https://doi.org/10.1016/j.applthermaleng.2024.123509.

[45] M. Silva, X. Liu, P. Hlaing, S. Sanal, E. Cenker, J. Chang, B. Johansson, H.G. Im, Computational assessment of effects of throat diameter on combustion and turbulence characteristics in a pre-chamber engine, Appl. Therm. Eng. 212 (2022), https://doi.org/10.1016/j.applthermaleng.2022.118595.

[46] A. Bianco, F. Millo, A. Piano, Modelling of combustion and knock onset risk in a high-performance turbulent jet ignition engine, Transp. Eng. 2 (2020), https://doi.org/10.1016/j.treng.2020.100037.

[47] F. Millo, L. Rolando, A. Piano, P. Sementa, F. Catapano, S.Di Iorio, A. Bianco, Experimental and numerical investigation of a passive pre-chamber jet ignition single-cylinder engine, in: Proceedings of the *SAE Technical Papers*, SAE International, 2021, https://doi.org/10.4271/2021-24-0010.

[48] Issa, R.I., "Solution of the implicitly discretised fluid flow equations by operator-splitting," 1985.

[49] V. Yakhot, S.A. Orszag, S. Thangam, T.B. Gatski, C.G. Speziale, Development of turbulence models for shear flows by a double expansion technique, Phys. Fluids A 4 (7) (1992) 1510–1520, https://doi.org/10.1063/1.858424.

[50] Convergent Science, "CONVERGE manual v3.0," 2020.

[51] J. Kim, R. Scarcelli, S. Som, A. Shah, M.S. Biruduganti, D.E. Longman, Assessment of turbulent combustion models for simulating prechamber ignition in a natural gas engine, J. Eng. Gas. Turbine Power. 143 (9) (2021), https://doi.org/10.1115/1.4050482.

[52] N. Morgan, A. Smallbone, A. Bhave, M. Kraft, R. Cracknell, G. Kalghatgi, Mapping surrogate gasoline compositions into RON/MON space, Combust. Flame 157 (6) (2010) 1122–1131, https://doi.org/10.1016/j.combustflame.2010.02.003.

[53] Wu, Y., Pal, P., Som, S., and Lu, T., "A skeletal chemical kinetic mechanism for gasoline and gasoline/ethanol blend surrogates for engine CFD applications," 2017.

[54] A. Piano, A. Scalambro, F. Millo, F. Catapano, P. Sementa, S.Di Iorio, A. Bianco, CFD-based methodology for the characterization of the combustion process of a

passive pre-chamber gasoline engine, Transp. Eng. 13 (2023), https://doi.org/10.1016/j.treng.2023.100200.

[55] E. Distaso, R. Amirante, E. Cassone, P.De Palma, P. Sementa, P. Tamburrano, B. M. Vaglieco, Analysis of the combustion process in a lean-burning turbulent jet ignition engine fueled with methane, Energy Convers. Manage 223 (2020), https://doi.org/10.1016/j.enconman.2020.113257.

[56] J. Antolini, P. Sementa, C. Tornatore, F. Catapano, B.M. Vaglieco, J.M. Desantes, J. J. López, Effect of passive pre-chamber orifice diameter on the methane combustion process in an optically accessible SI engine, Fuel (2022), https://doi.org/10.1016/j.fuel.2022.126990.